The Retrieval of Effective Particle Radius and Liquid Water Path of Low-Level Marine Clouds from NOAA AVHRR Data

MAKOTO KUJI

Department of Information and Computer Sciences, Nara Women's University, Nara, Japan

TADAHIRO HAYASAKA AND NOBUYUKI KIKUCHI

Center for Atmospheric and Oceanic Study, Tohoku University, Sendai, Japan

TERUYUKI NAKAJIMA

Center for Climate System Research, University of Tokyo, Tokyo, Japan

MASAYUKI TANAKA

Center for Atmospheric and Oceanic Study, Tohoku University, Sendai, Japan

ABSTRACT

An algorithm was developed to retrieve both the optical thickness and the effective particle radius of low-level marine clouds simultaneously from National Oceanic and Atmospheric Administration Advanced Very High Resolution Radiometer (AVHRR) data. The algorithm uses the combination of the visible (channel 1) and the middle-infrared (channel 3) reflected radiation. The thermal component in the middle infrared was corrected with the thermal-infrared (channel 4) radiance by a statistical technique using a regressive formula. The liquid water path (i.e., vertically integrated liquid water content) was also estimated as a by-product. The algorithm was applied to AVHRR datasets for which almost-synchronized airborne observations were conducted around the First International Satellite Cloud Climatology Project (ISCCP) Regional Experiment (FIRE) and the Western North Pacific Experiment (WENPEX) regions. The two regions are different in the characteristics of cloud fields: summer stratus and stratiform clouds that result from outbreaks of cold air mass over the warm sea in winter seasons, respectively.

In the FIRE region, the retrieved parameters are almost consistent with those of in situ airborne observations, even when using a more practical approach than the algorithms adopted in previous studies, but there is still a discrepancy between the satellite-derived results and those of in situ airborne observations around the drizzle-dominated portion. In the WENPEX region, it is suggested that cloud fractional coverage in a pixel may cause error in the retrieval, particularly for horizontally inhomogeneous cloud field analyses with an assumption of a plane-parallel atmospheric model. It is found also that the thermal-infrared information has a potential to estimate the inhomogeneity of cloud fields as a result of the comparison between stratus and broken cloud cases.

1. Introduction

Clouds play a crucial role in the earth's climate, particularly in its global energy budget and water circulation. It therefore is important to understand optical, microphysical, and liquid water properties. Data remotely sensed by satellites are very useful for observation of clouds that have great spatial and temporal variations on both global and regional scales.

Studies on the retrieval of the cloud optical thickness and the effective particle radius using airborne or spaceborne measurements began in the 1970s. Hansen and Pollack (1970) indicated the retrieval possibility of the size of cloud particles and their phase (liquid or solid) as well as the total optical depth of clouds from reflectivity observations. Curran and Wu (1982) investigated cloud optical thickness, thermodynamic phase, and effective particle size using the Skylab near-infrared channel observations. They also investigated cloud-top temperature from the thermal-infrared channel. Twomey and Cocks (1982) made the comparison between the calculated and observed reflectance for clouds in which microphysical and liquid water properties were esti-

---

Corresponding author address: Makoto Kuji, Dept. of Information and Computer Sciences, Faculty of Science, Nara Women's University, Nara 630-8506, Japan.
E-mail: makato@ics.nara-wu.ac.jp

mated from in situ measurements. Both results showed discrepancies that could not be resolved. The retrieval of cloud fraction within field of view (FOV), optical thickness, cloud-top temperature, and microphysical model parameters with the National Oceanic and Atmospheric Administration (NOAA) Advanced Very High Resolution Radiometer (AVHRR) channels was studied by Arking and Childs (1985). Rawlins and Foot (1990) retrieved the cloud optical thickness and the effective droplet radius simultaneously and found that the retrieved effective droplet radius is larger than that of in situ measurement by 50%. Nakajima and King (1990) also developed a retrieval algorithm of the cloud optical thickness and the effective droplet radius simultaneously. This algorithm was applied to the data of the Multichannel Cloud Radiometer (MCR) on a National Aeronautics and Space Administration (NASA) ER-2 aircraft to retrieve the cloud optical thickness, the effective droplet radius, and the liquid water path (Nakajima et al. 1991). The retrieved results generally were comparable with in situ particle measurements in magnitude, and the remotely sensed effective particle radius was systematically larger, by a few micrometers, than the effective particle radius of in situ measurements. Taylor (1992) showed that LOWTRAN 7 (low-resolution transmittance model and code) was better than LOWTRAN 5 for estimating gaseous absorption for particle radius retrieval in the near-infrared spectral region. Platnick and Twomey (1994) analyzed the AVHRR data to retrieve the cloud optical thickness and discussed the cloud susceptibility. Hayasaka et al. (1994) investigated the utility of AVHRR data to retrieve the cloud optical thickness and compared the calculated and observed shortwave radiative flux, which showed good consistency. Near-global analyses of the cloud optical thickness and the effective particle radius were carried out by Han et al. (1994), using the International Satellite Cloud Climatology Project (ISCCP) Global Area Coverage (GAC) data. Nakajima and Nakajima (1995) have developed an algorithm to retrieve simultaneously the cloud optical thickness and the effective particle radius from the AVHRR data for global analyses as well as for the First ISCCP Regional Experiment (FIRE) and Atlantic Stratocumulus Transition Experiment regions.

In this paper, an algorithm to retrieve the cloud optical thickness and the effective particle radius simultaneously from AVHRR data is presented. A validation comparison with in situ observations also was done. In the second section, the analyzed AVHRR data and in situ airborne observations used for the validation are described. The analyzed cloud field is different seasonally and spatially, and those cloud fields contain several kinds of cloud such as stratus, stratocumulus, and cumulus. In the third section, the algorithm developed in this study is described. The algorithm uses the visible and middle-infrared reflected solar radiance. The thermally emitted component of the middle infrared is corrected by the thermal-infrared radiance emitted by the

earth–atmosphere system; Nakajima and Nakajima (1995) corrected this undesirable thermal component with iterative calculations. There are several truncations to reduce calculation time on a scan geometry and a response filter function in this study. The retrieved results are described in the fourth section, and discussions about a partial cloud problem that potentially may influence the algorithm are made in the fifth section by comparing with airborne observations. Last, a summary is presented in the sixth section.

2. Data description and in situ observation

In this section, the AVHRR datasets used in this study are described. We analyzed the AVHRR Local Area Coverage (LAC) data, which observed the different types of low-level marine clouds in two regions: the western North Pacific Ocean area in winter observed by *NOAA-11* and the area off the coast of California in summer observed by *NOAA-10*. We also will describe the in situ airborne observation data that were used to validate the satellite-retrieved results.

a. Western North Pacific Experiment (WENPEX) region

During the period from 10 to 27 January 1991, Western North Pacific Experiment (WENPEX) intensive cloud observations were conducted around the Amami–Ooshima Islands (28°N, 160°E) (Fujiyoshi et al. 1995; Hayasaka et al. 1995; Ishizaka et al. 1995). A stratus, stratocumulus, and cumulus cloud system extends over the East China Sea, located between the Siberian high pressure system and the Pacific low pressure system in the winter season in the east Asian area.

Table 1 shows the flight area, including all the flight lines and the line synchronized to *NOAA-11* AVHRR observations. The intensive field observation campaign was conducted with two Cessna 404 Titan aircraft. They observed optical, microphysical, and liquid water properties such as the upward and downward radiative fluxes with pyranometers from one aircraft above the cloud top (called aircraft A) and another aircraft (aircraft B) in and below the cloud, effective particle radius with a Particle Measuring Systems, Inc., Forward-Scattering Spectrometer Probe (FSSP) from aircraft B in the cloud layer, and liquid water path with a microwave radiometer from aircraft A, respectively. The details are described for the radiative flux observation by Hayasaka et al. (1994, 1995), the FSSP observation by Ishizaka et al. (1995), and the microwave radiometry observation by Fujiyoshi et al. (1995).

Figure 1 illustrates the imagery of *NOAA-11* AVHRR data of 16 January 1991, with normalized gray level for each of five channels and all of the six flight areas surrounded by the smaller rectangles (45 × 52 pixels; about 50 km × 57 km at the surface). Because the projection of this imagery is the Mercator, latitude and

TABLE 1. Airborne observation of WENPEX campaign.

Date	Time (JST[a])	Northwest, or flight start (°N, °E)	Southeast or flight end (°N, °E)	Flight
16 Jan 1991	1310–1503	28.850, 130.667	28.328, 131.167	Area[b] (six lines)
	1413–1427	28.292, 131.107	28.303, 130.400	Fourth[c] line
	1417:04	28.589, 130.917	28.589, 130.917	AVHRR[d]
18 Jan 1991	1330–1446	29.808, 128.833	29.145, 129.003	Area[b] (four lines)
	1348–1358	29.200, 128.498	29.340, 128.512	Second[c] line
	1355:04	29.477, 128.918	29.477, 128.918	AVHRR[d]
27 Jan 1991	1310–1454	29.082, 128.000	28.828, 129.060	Area[b] (six lines)
	1347–1356	29.001, 128.400	29.000, 129.060	Fourth[c] line
	1355:09	28.955, 128.530	28.955, 128.530	AVHRR[d]

[a] JST = Japan Standard Time.
[b] "Area" corresponds to the analyzed area in AVHRR imageries, which contains all flights (northwest and southeast).
[c] The nth flight line (start to end) is the synchronized observation with NOAA AVHRR.
[d] The rows with "AVHRR" in the flight column show the passing time of the NOAA satellite over the center of the area each day.

longitude of the northwest location in Table 1 indicate the top left of the smaller rectangles and the southeast location indicates the bottom right of them. The area observed by aircraft was covered over by an extensive low-level marine cloud system over a warm sea surface. The analyzed area is located around the center of the AVHRR imagery for 16 January 1991 and is around the off-center portion for 18 and 27 January 1991. The size of the analyzed area is 16 × 67 (16 × 74) and 95 × 27 (98 × 28) pixels (km at the surface) for 18 and 27 January 1991, respectively.

b. FIRE region

From June to July 1987, the FIRE Marine Stratocumulus Intensive Field Observation (MS-IFO) was conducted off the coast of California (Albrecht et al. 1988).

The NOAA-10 AVHRR data targeting the area off the coast of California were used to retrieve the cloud optical, microphysical, and liquid water properties. The dates analyzed in this study were 7, 10, and 16 July 1987. The observation times were around 1640 UTC, and the airborne observation was conducted approximately 1 h after the satellite observations of each date. We cut out and analyzed the AVHRR data for the area in which airplane observations were conducted during FIRE MS-IFO. Table 2 indicates the start and finish locations of the center line in the area of the analyzed AVHRR data. The center line corresponds to the MCR and C-131A flight leg, and the area corresponds to the area in which MCR made a scan observation. The area is 35 × 77 pixels (about 96 km × 104 km) for 7 July, 35 × 125 pixels (about 68 km × 145 km) for 10 July, and 19 × 128 pixels (about 59 km × 141 km) for 16 July 1987. All the data are located around the off-center portion of the satellite imagery. The details of the airborne observations can be found in Albrecht et al. (1988) and Nakajima et al. (1991).

3. Retrieval algorithm

The details of the retrieval algorithm are described in this section. The algorithm was developed on the basis of the optical properties of water droplets and the AVHRR channel specifications. We adopted a realistic approach for the radiative transfer calculations and the correction of the thermal component of AVHRR channel (ch.) 3. The degradation of the calibration constants for AVHRR ch. 1 was corrected also.

a. Analysis flow

The schematic diagram of analysis flow is shown in Fig. 2. We used the three channels of the NOAA AVHRR radiance data, that is, ch. 1 (visible), ch. 3 (middle infrared), and ch. 4 (thermal infrared). Channel 4 is used for the correction of the thermal radiance component of ch. 3. We assumed the plane-parallel model atmosphere to make the lookup table and retrieve the optical thickness of cloud and the effective radius of droplets simultaneously. Last, the liquid water path, that is, the vertically integrated liquid water content, was derived from the above-two cloud parameters as a byproduct.

b. Principle of the algorithm

NOAA AVHRR ch. 1 has the response function in the visible spectral region (Kidwell 1991). In this spectral region, the cloud reflectivity is governed by optical thickness τ_c but is almost independent of droplet size information because the imaginary index of refraction of liquid water is extremely small (on the order of 10^{-9}; Hale and Querry 1973). Gaseous absorption in the cloud layer and in the above layer is very small except for the ozone Chappuis band.

NOAA AVHRR ch. 3, on the other hand, has the response function in the middle-infrared spectral region (Kidwell 1991). The observed radiance in this spectral
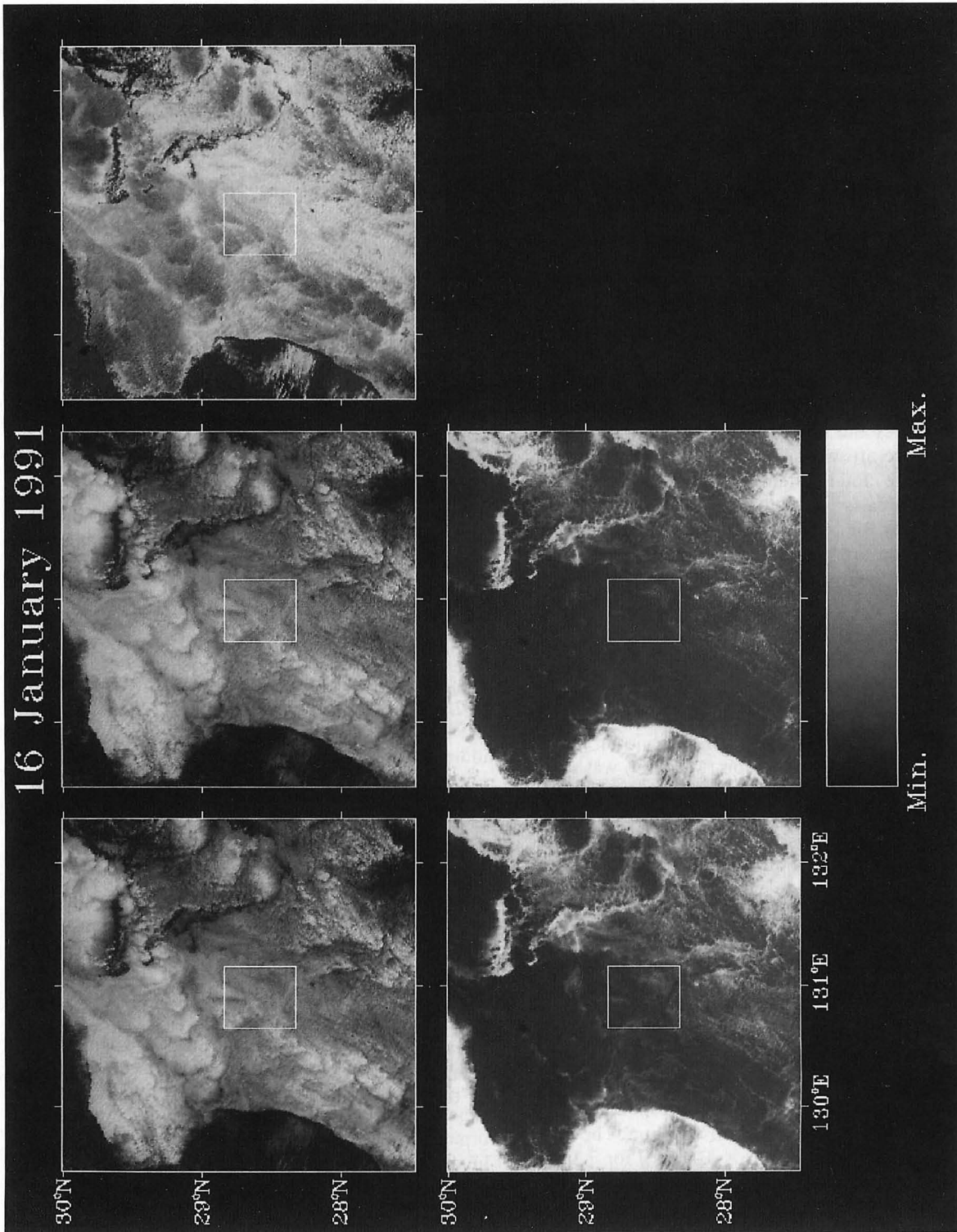
FIG. 1. Imagery of AVHRR data (16 Jan 1991). From upper left to lower right: ch. 1, ch. 2, ch. 3, ch. 4, and ch. 5. Level slice is normalized between minimum value (black) and maximum value (white) for each channel. Center frame of each image indicates the analyzed area (45 × 52 pixels on this date).

TABLE 2. AVHRR and C-131A observation during FIRE MS-IFO.

Date	Time (PDT*)	Start (°N, °W)**	End (°N, °W)**	Sensor
7 Jul 1987	0944	31.97, 122.26	31.08, 121.91	AVHRR
10 Jul 1987	0838	31.86, 121.40	31.20, 120.08	AVHRR
	0922–0951	31.84, 121.37	31.22, 120.10	C-131A
16 Jul 1987	0948	30.82, 121.21	32.07, 120.94	AVHRR

* PDT = Pacific Daylight Time.
** The start to end for AVHRR corresponds to the center line of the analyzed region.

band is influenced by both cloud droplets' absorption (Downing and Williams 1975) and gaseous absorption in the cloud layer, the above-cloud layer, and the sub-cloud layer. The photons in the cloud layer also undergo multiple scattering so that the observed radiance of ch. 3 is attenuated by cloud droplets' and gaseous absorption through the cloud layer by the multiple scattering process. In general, the scattering processes are related to the cross section of droplets, and the absorption is related to the volume of droplets. The following effective particle radius is therefore a representative statistical parameter for the cloud droplets. The effective particle radius r_e is defined as follows (Hansen and Travis 1974):

$$r_e \equiv \frac{\int_{r_1}^{r_2} r \pi r^2 n(r)\, dr}{\int_{r_1}^{r_2} \pi r^2 n(r)\, dr}, \qquad (1)$$

where the numerator is proportional to the gross droplet volume and the denominator is equivalent to the cross section. For the cloud droplet size distribution $n(r)$ in Eq. (1), the number lognormal size distribution is used according to Nakajima and King (1990).

The observed radiance of ch. 3, which undergoes multiple scattering, thus contains information on the cloud droplet size, and the radiance of ch. 1, with little absorption, is dominated by the total droplet cross section in the cloud layer. It therefore is expected that, if the effective droplet radius is larger, the absorption by the cloud layer is stronger, and the observed radiance of ch. 3 consequently is lower.

We used an approximation formula to derive the liquid water path L from the retrieved optical thickness τ_c and effective particle radius r_e (Stephens 1978):

$$L \approx \frac{2}{3} \tau_c r_e \rho_w, \qquad (2)$$

where ρ_w is the density of water.

c. Model atmosphere

A four-layer atmospheric model was used for the analysis, as described in Table 3. Atmospheric molecules' absorption and scattering were considered at all layers. The top layer was assigned as the stratosphere and above to act as a filter for ozone absorption. The cloud layer is imbedded as a plane-parallel one in the third layer. Although the clouds in the real atmosphere have various
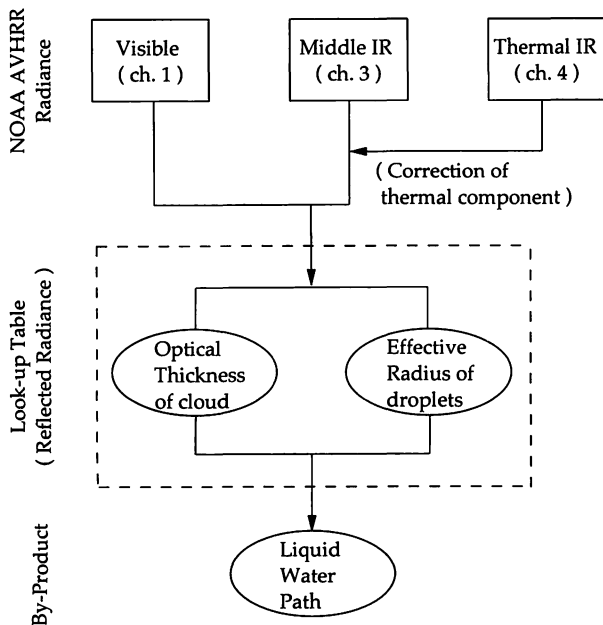
FIG. 2. Schematic diagram of analysis flow. Inversion procedure with a lookup table method. The lookup table is prepared for the solar reflected radiance so that the AVHRR ch.-3 (middle infrared) thermal component is removed using the ch.-4 data (thermal infrared). Liquid water path is estimated from the retrieved optical thickness and effective particle radius as a by-product.

TABLE 3. Atmospheric model.

Layer	Components (Common)	Gaseous absorption	
		Ch. 1	Ch. 3**
1	Stratosphere and above (Rayleigh scattering)	Ozone	USSA*
2	Layer above cloud (Rayleigh scattering)	—	USSA*
3	Cloud layer (Rayleigh scattering)	—	Water vapor
4	Layer under cloud (Rayleigh scattering)	—	USSA*
Boundary	Sea surface (Lambertian; albedo 0.06)	—	—

* USSA = U.S. Standard Atmosphere, 1976 incorporated in LOW-TRAN 7.
** Ozone is not taken into account because of little absorptance in ch. 3.

shapes, the low-level marine stratus and stratocumulus clouds are, in general, better treated as a plane-parallel cloud model among the various cloud types. The lower boundary was sea surface and was treated as Lambertian with an albedo of 0.06.

The *U.S. Standard Atmosphere, 1976,* which is incorporated in LOWTRAN 7, was referred to for gaseous, atmospheric temperature, and atmospheric pressure profiles at all layers in principle. Below 3 km, radiosonde data obtained at the Naze Observatory of the Japan Meteorological Agency were referenced for water vapor, atmospheric temperature, and atmospheric pressure profiles to set the several atmospheric parameters in the model atmosphere. Ozonesonde measurements made at the Kagoshima and Naha Observatories of the Japan Meteorological Agency were used for the calculation of Chappuis band absorption. Only the ozone Chappuis band was taken into account for the gaseous absorption in ch. 1, and all the relevant gaseous absorptions were included in ch. 3. Gaseous absorption due to ozone is ignored in the ch.-3 spectral region for it is of little importance.

Gaseous absorption in the multiple-scattering process of the cloud layer was treated by using the correlated k adopted by LOWTRAN 7. It is expressed by the following equation:

$$\mathcal{T}(u) = \sum_{i=1}^{3} w_i e^{-k_i U(P,T,u)}, \qquad (3)$$

where $\mathcal{T}(u)$ is the transmittance with the absorption molecule amount u, and w_i and k_i are the weight and the corresponding absorption coefficient, respectively. Here, U is the absorption molecule amount scaled by the air pressure P, air temperature T, and u (Pierluissi and Tsai 1987; Pierluissi et al. 1989).

d. Lookup table calculation

Both ch.-1 and ch.-3 reflected radiance as observed by satellite were calculated to make the lookup table, as shown in Fig. 2, changing cloud optical thickness and effective particle radius. Reference to the computer code LOWTRAN 7 allowed us to determine the spectral intervals at which we made the calculations. Its spectral resolution is nominally 5 cm^{-1}. The ch.-1 spectral region, 0.54–0.80 μm (12 500–18 515 cm^{-1}) then was divided into 1204 spectral intervals. The ch.-3 spectral region, 3.5–4.1 μm (2440–2855 cm^{-1}) also was divided into 84 spectral intervals. The radiative transfer calculation was executed, based on Nakajima and Tanaka (1986, 1988).

For ch. 1, the radiative transfer calculation was made once at the central wavelength of each AVHRR response function instead of over the whole spectral region to avoid a time-consuming process. The monochromatic calculation of ch.-1 radiance is sufficient for the retrieval of cloud optical thickness, as shown by Hayasaka et al.

TABLE 4. Scan geometry.

Date	μ_0^a	μ^b	$\Delta\phi^c$
16 Jan 1991	0.553	1.000	—
18 Jan 1991	0.591	0.722	52.4
27 Jan 1991	0.629	0.701	59.1
7 Jul 1987	0.692	0.580	18.15
10 Jul 1987	0.513	0.816	163.4
16 Jul 1987	0.706	0.485	16.76

[a] μ_0 = cosine of solar zenith angle.
[b] μ = cosine of satellite zenith angle.
[c] $\Delta\phi$ = relative azimuthal angle between the sun and satellite in degrees.

(1994) in detail. For ch. 3, on the other hand, the radiative transfer calculation of the 84 spectral intervals weighted by the response function was made, because the complicated gaseous absorption lines are effective even in such a narrow bandwidth. Solar spectral intensity also was considered, after Thekaekara (1974). For simplification, the calculation geometry in Table 4 is used at the latitudinal and longitudinal central location in the analyzed target area instead of at each pixel. It is sufficient, however, to make a lookup table for the analyzed area in this study because the difference of the scan geometry is almost identical between the center of an image and the corner of an analyzed area, and the relative error in the calculated radiance is less than 0.3% for 16 January 1991, for instance.

e. Calibration constants

We assumed that the relative shape of the spectral response function of AVHRR ch. 1 had not changed from the prelaunch one and that all observed changes in AVHRR response in orbit were attributable to changes in gain and deep-space count. We took into account *NOAA-11* AVHRR degradation in ch. 1 according to the estimation of Los (1993). For *NOAA-10* AVHRR data in the FIRE region, on the other hand, we used the calibration correction method proposed by Teillet et al. (1990).

f. Thermal emission correction

NOAA AVHRR ch. 3 has the response function near 3.7 μm, to which is contributed by both the reflected solar radiation and the thermally emitted radiation of the earth–atmosphere system. Because the calculations for the lookup table in Fig. 2 are made only for the reflection of solar radiation, it is necessary to correct the thermal emission. The following method was used for this purpose.

NOAA AVHRR ch. 4 has the response function near 11 μm, which observes only thermal emission from the earth–atmosphere system by day and night. NOAA AVHRR ch. 3 also observes only thermal emissions at night. It therefore is possible to make a regression curve
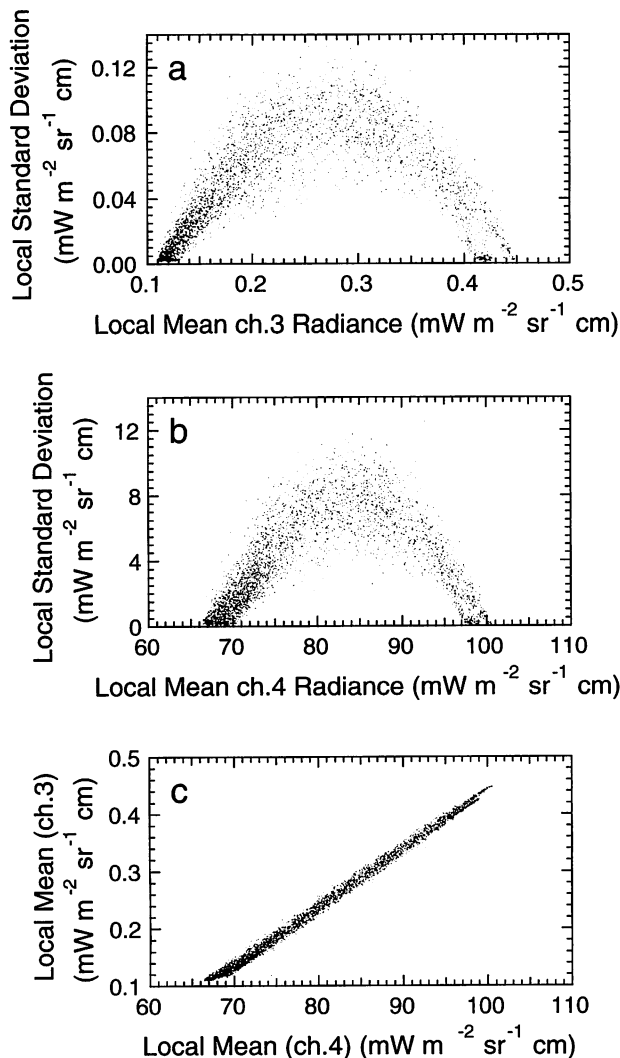
FIG. 3. Arch structure of thermal channels of AVHRR (nighttime). Relationship of the local mean ± standard deviation at both ch. 3 and ch. 4 of AVHRR. The 15 Jan 1991 data from *NOAA-11* around the Amami–Ooshima Islands (28°N, 160°E). (a) Relationship between local mean ch. 3 and standard deviation for 4 × 4 pixels. (b) As in (a) but for ch. 4. (c) Relationship between local mean ch. 4 and ch. 3.

between ch. 3 and ch. 4 for thermal emissions at night. This regression curve was determined by using only groups of pixels that exhibit spatially uniform emission, from all those averaged during the observational period. We selected those pixels using the spatial coherence method (Coakley and Bretherton 1982). The observed radiance of ch. 3 in the daytime contains both the solar reflected and thermally emitted components, as mentioned above. The solar reflected component in the ch.-3 radiance data was obtained by using the regression curve that relates the ch.-3 component to that of ch. 4.

An example of the relationship between ch.-3 thermal radiation and ch.-4 thermal radiation obtained from the actual satellite data is shown in Fig. 3. Both ch.-3 (Fig. 3a) and ch.-4 (Fig. 3b) data show an arch structure. It

is likely that the leg of the arch at the higher mean radiance portion represents sea surface regions and the one at the lower mean radiance portion represents cloud regions. Figure 3c also shows a good positive correlation of the local mean radiance between ch. 3 and ch. 4. According to Coakley and Davies (1986), the following relationship between the ch.-3 and ch.-4 thermal radiance is obtained

$$I_3 = aI_4^b, \qquad (4)$$

where I_3 and I_4 are the radiance observed at ch. 3 and ch. 4, respectively. The coefficients a and b are determined statistically. From Figs. 3a, b, it is found that the region at the arch top corresponds to the more-inhomogeneous pixels that include cloud and sea area. It is necessary to pick out the pure pixels that are composed of a single component, for example, only cloud, in order to determine the coefficients in Eq. (4). The data that have a local standard deviation of less than 0.01 and 2 mW m^{-2} sr^{-1} cm for ch. 3 and ch. 4 were chosen simultaneously. Because this algorithm is for the lower water cloud, the data for the local mean radiance greater than or equal to 0.1 and greater than or equal to 60 mW m^{-2} sr^{-1} cm for ch. 3 and ch. 4, respectively, were selected simultaneously as well. As a result of the above process, we selected the 14 data from the three nighttime scenes (256 × 256 pixels for 16, 18, and 27 January 1991) of *NOAA-11* from the WENPEX region and determined the coefficients in Eq. (4) as a is 8.33 × 10^{-8} and b is 3.36 in the WENPEX case. For the FIRE case, on the other hand, a is 9.36 × 10^{-12} and b is 5.32 using the one nighttime scene (256 × 256 pixels for 26 July 1987) of *NOAA-10* from the WENPEX region instead of the FIRE region because of the limitation of the nighttime data acquisition.

Once the regression equation is determined, the reflected component of ch.-3 radiance for the daytime data is obtained. Figure 4 shows an example of this process. Figure 4a illustrates the relationship between ch.-3 and ch.-4 radiance for nighttime data without locally averaging, as well as the thermal correction curve as determined by the above process. The relationship between ch.-3 and ch.-4 daytime data is shown in Fig. 4b with the thermal correction curve. After the extraction of the thermal component from the ch.-3 daytime data using the ch.-4 daytime data, the reflection component of ch.-3 radiance is obtained as shown in Fig. 4c. The thermally corrected data of AVHRR ch.-3 thus obtained are used for the retrieval process in this study.

4. Retrieval results

In this section, we will describe the simultaneous retrieval of the cloud optical thickness and the effective particle radius by the calculated lookup table and the retrieved cloud physical values for the WENPEX and FIRE regions. The retrieved results also were compared with the in situ airborne observations.
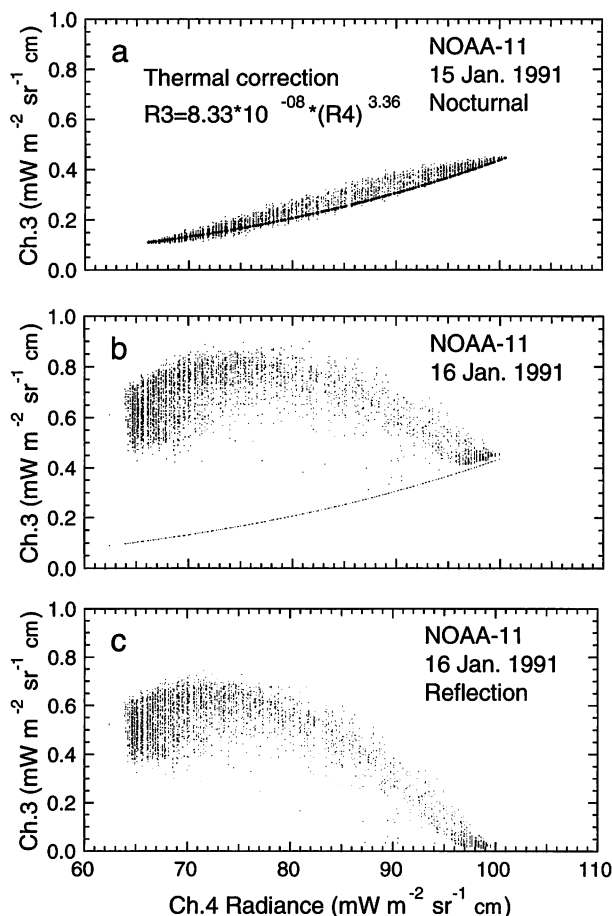
FIG. 4. Extraction of thermal component from daytime ch. 3. Removal of the thermal component from daytime ch. 3 using the regressive curve between ch. 3 and ch. 4 with the daytime ch. 4 (thermal component only). (a) Regressive curve between ch. 3 and ch. 4 at nighttime after the pure pixel threshold of the local standard deviation for both ch. 3 and ch. 4. (b) Relationship between ch. 3 and ch. 4 before thermal correction. (c) Extracted reflection component of ch. 3.

a. WENPEX region

For the WENPEX region, *NOAA-11* made coincident observations to the flights on 16, 18, and 27 January 1991. Figure 5 illustrates the calculated lookup table chart and actual satellite data after the thermal correction for the case of 16 January 1991. This figure gives us information about the relationship between the optical thickness of the cloud and the effective droplet radius and the observed radiance on ch. 1 and ch. 3. The scan geometry in this case indicates that *NOAA-11* AVHRR made a nadir observation, and that the solar zenith angle was around 56°. It is indicated that the optical thickness of cloud is correlated well with the ch.-1 radiance, and the effective particle radius does not correspond to the reflected ch.-3 radiance straightforwardly. The area of the small radiance for ch. 1, that is, the small optical thickness of clouds in the lookup table chart, does not give information on the effective particle radius because of the degradation of the calculated curves, whereas a

good determination of the effective particle radius is achieved with a large value of the ch.-1 radiation where optical thickness is larger than 4. Figure 5 suggests that the retrieved effective radius is about 2.8–6.6 μm and the retrieved optical thickness of clouds is actually about 4–128 in this case.

Figures 6 and 7 show the distributions of the effective particle radius and the liquid water path, respectively, retrieved for 16 January 1991. It is found that the range of the effective particle radius in many portions is about 4–5 μm from Fig. 6 and the range of the liquid water path is about 30–70 g m^{-2}, from Fig. 7. The area in which the effective particle radius is larger corresponds to that of the higher liquid water content. Hayasaka et al. (1994) has discussed the optical thickness of cloud around this region.

Figure 8 illustrates the joint probability density function between the effective particle radius and the liquid water path for 16 January 1991. It is found that the positive linear correlation between the effective radius and the liquid water path is represented by a logarithmic scale. The mode value falls to about 4.0 μm for the effective particle radius. There is a mode value near 30 g m^{-2} for the liquid water path. This linear tendency shows the typical development for low-level marine stratus or stratocumulus cloud in a cold air mass over a warmer sea surface. It suggests that the deeper clouds tend to produce larger droplets at cloud top. The values of effective particle radius and liquid water path as a by-product in Fig. 8 as well as in the following Table 5 are adjusted to the middle-level values over the cloud layers after Nakajima and King (1990) and Nakajima and Nakajima (1995).

The regional statistics (mean ± standard deviation) of the optical thickness of clouds, the effective particle radius, and the liquid water path of the analyzed region for all three days (16, 18, and 27 January 1991) are summarized in Table 5. These results for low-level marine clouds near Japan in winter are larger for the optical thickness and smaller for the effective particle radius, respectively, in comparison with near-global statistical analyses using AVHRR GAC data (Han et al. 1994; the Northern Hemisphere case in winter over ocean in Table 6).

b. FIRE region

For this region, *NOAA-10* made the observations coincidently to the airborne radiative and microphysical measurements that enabled us to make a validation for the retrieval algorithm with FIRE regional data. The airborne data were acquired during FIRE IFO. The NASA ER-2 MCR performed the radiation observations from the nominal 18-km height, while the Washington University C-131A PMS probes [FSSP-100 and Optical Array Probe (OAP-200X) cloud probes and OAP-200Y precipitation probe] observed the microphysical properties in and around the cloud decks. The ER-2 MCR is the multispectral radiometer on board, with a cross-
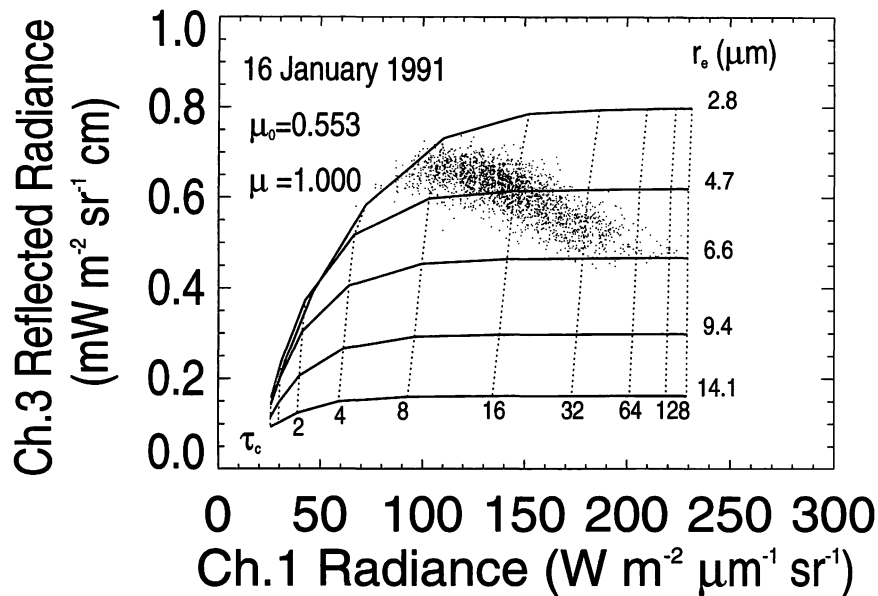
FIG. 5. Simultaneous decision chart (lookup table; solid and dashed lines) with actual AVHRR data (dots). The ordinate of this figure is the observed reflected radiance in ch. 3, and the abscissa is the observed ch.-1 radiance. The calculations for the model atmosphere were carried out for scan geometry at the center of the relevant analyzed area; the cosine of the solar zenith angle (μ_0) is 0.553, and the cosine of the satellite zenith angle (μ) is 1.000 corresponding to 16 Jan 1991. The solid lines mean the theoretical calculations with the cloud optical thickness changed and the cloud droplet effective particle radius fixed, and the dashed lines represent the reverse relationships between the cloud optical thickness and the effective particle radius. The lookup table thus was made for the case of the cloud optical thickness (τ_c): 0.5, 1, 2, 4, 8, 16, 32, 64, 128, and 256, and the effective particle radius [r_e (μm)]: 2.8, 4.7, 6.6, 9.4, and 14.1. The scattered dotted data are the actual satellite data.

tracking scan, the same as NOAA AVHRR but with a smaller area of observation than that of the satellite. The C-131A PMS probes measured microphysical properties such as the cloud droplet radius distribution at the cloud top and bottom. Nakajima et al. (1991) made a detailed analysis of these two airborne observations. They suggested that the discrepancy of the effective particle radius between remotely sensed and in situ microphysical measurements depends upon the uncertainty due to the unknown water vapor continuum absorption in the near-infrared spectral regions. The atmospheric correction based on LOWTRAN 7, instead of one based on LOW-TRAN 5 that was adopted by Nakajima et al. (1991), may diminish this systematic discrepancy (Taylor 1992).

Figure 9 shows the AVHRR-retrieved results and the comparison with in situ airborne observations. Figure 9a illustrates the retrieved results of the optical thickness of clouds along with the ER-2 flight distance, which is almost the same as the C-131A flight leg. It also contains the optical thickness of clouds derived from in situ microphysical observations by the C-131A. The retrieved results in this study coincide well with those of the in situ observation. Figure 9b illustrates the retrieved results of the effective particle radius, which are relatively consistent with those obtained by in situ observations. After the correction of results so as to compare the effective particle radius from AVHRR data with those

observed by in situ PMS probes in the middle height within the cloud layer, a good coincidence in magnitude and spatial variations was obtained. The results from both 0 to 30 km and near 40 km in flight distance do not agree well with the in situ measurements, however. It is suggested that the discrepancy was due to the drizzle-sized particles at the lower portion of the cloud layer in these regions (Nakajima and Nakajima 1995). The satellite measurement is insensitive to the lower portion of the cloud layer, and, furthermore, the assumed model profile, so as to adjust the satellite-retrieved effective particle radius to the comparable value at the level of the PMS probes' measurement, did not fit the drizzle-sized particles in this case (Nakajima et al. 1991). The retrieved results of the liquid water path are illustrated in Fig. 9c, where the values derived from the retrieved results are in good coincidence with the in situ Johnson–Williams hot-wire probe observations. These three comparisons suggest that the algorithm developed in this study is very useful in retrieving the optical thickness of clouds and the effective particle radius simultaneously, as well as the liquid water path as a by-product.

The results from in situ observation, such as the optical thickness of a cloud layer, the effective particle radius, and the liquid water path, were estimated as follows. A vertical flight was carried out to measure liquid water content at several levels within the cloud layer so as to
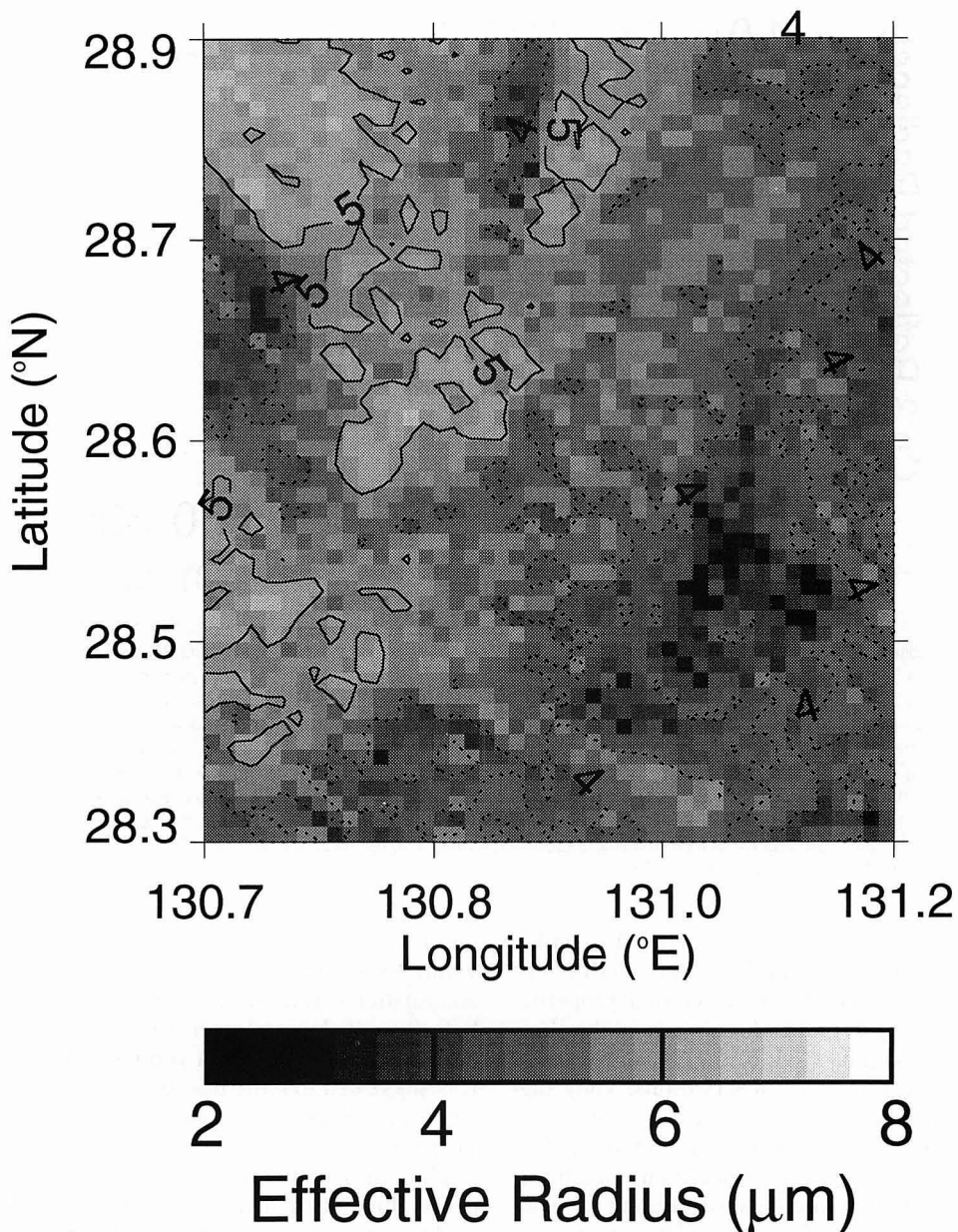
FIG. 6. Contour map of the retrieved effective particle radius for 16 Jan 1991 for the area in which the airborne observations were made. The units of the contour labels are micrometers.

estimate the liquid water path. Effective geometrical thickness was determined from dividing the liquid water path by the liquid water content at the level where the level (horizontal) flight measurement was carried out with the Johnson–Williams hot-wire probe. In this case, the effective geometrical thickness was determined to be 400 m. The in situ liquid water path for the level (horizontal) flight, which was compared to the AVHRR retrieved result, was estimated as the product of the effective geometrical thickness (400 m) and the liquid water content measured with the Johnson–Williams hot-wire probe. The in situ optical thickness, which also was compared to the

AVHRR retrieved result, was estimated from the in situ liquid water path and the in situ effective particle radius measured with the PMS probes using a relationship the same as Eq. (1).

The in situ measurements for cloud microphysics were carried out with the PMS probes for the effective particle radius and the Johnson–Williams hot-wire probe for the liquid water content. The liquid water content could be estimated from the PMS probes' measurements. The magnitude of the liquid water content derived from integration of PMS-derived size distribution measurements, however, was significantly lower than
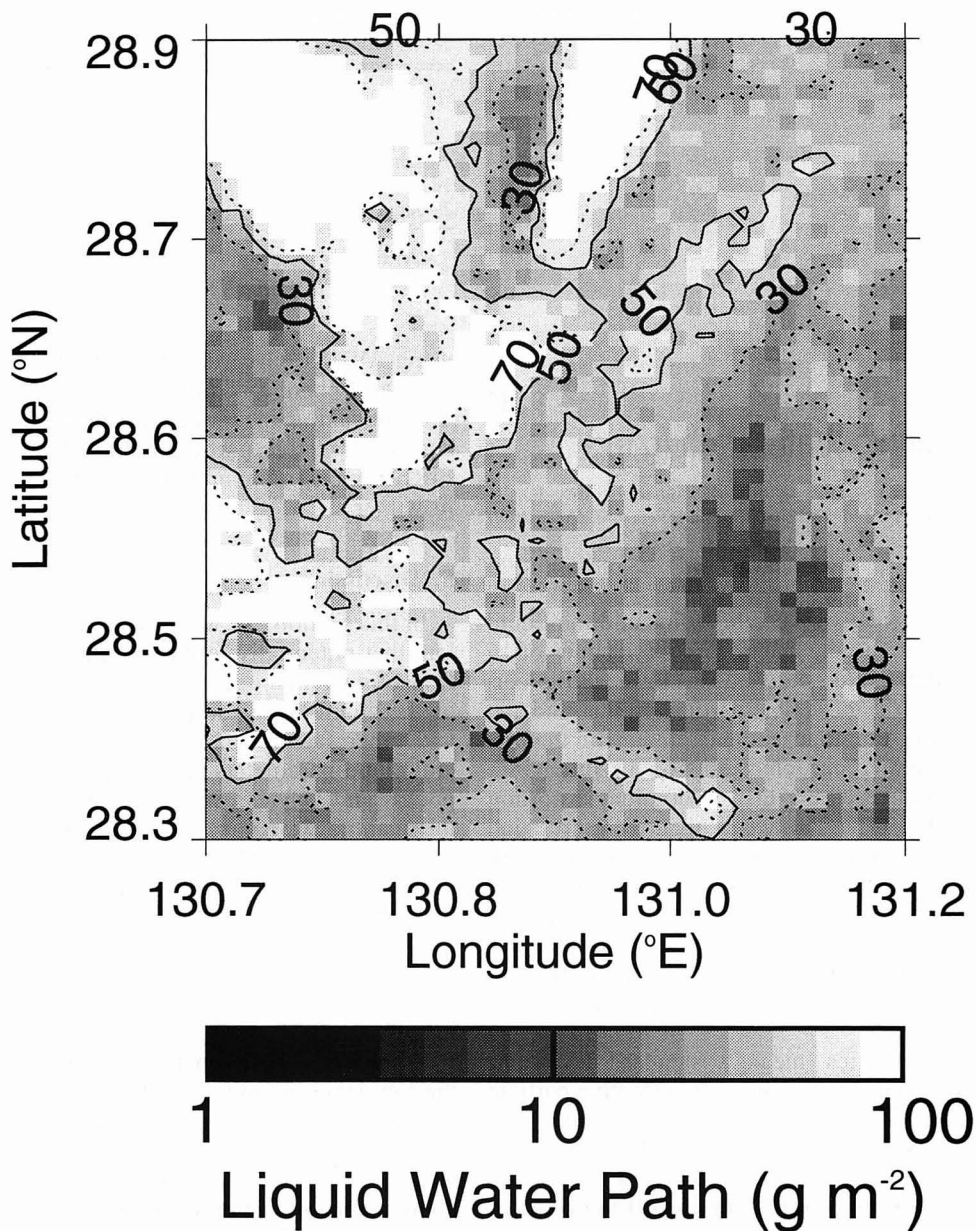
FIG. 7. As in Fig. 6 but for the liquid water path. The units of the contour labels are grams per meter squared.

corresponding measurements obtained with the John-son–Williams hot-wire probe (Nakajima et al 1991). FSSP, in principle, measures the forward-scattering intensity with incident laser and the pulse counts so as to estimate the particle size and the number concentration. The liquid water content is derived indirectly with FSSP accordingly. The Johnson–Williams hot-wire probe, on the other hand, measures heat loss accompanied with liquid water particles making contact to a hot wire. The heat loss is directly relevant to the liquid water amount. Consequently, it seemed feasible to adopt the liquid water content estimated with the Johnson–Williams hot-wire probe rather than with the FSSP in this case.

Figure 10 illustrates the joint probability density function between the effective particle radius and the liquid water path for three analyzed days (7, 10, and 16 July 1987). The distribution of contour lines is similar to the results remotely sensed by MCR (Nakajima et al. 1991). The contour lines of 7 July 1987 show the positive correlation between the effective particle radius and the liquid water path (the correlation coefficients are shown in Table 5). This relationship also was seen in Fig. 8, which is the retrieval result for the low-level marine stratus in the WENPEX region in winter from *NOAA-11* AVHRR. This positive relationship may be typical for stratus cloud systems; that is, as a cloud layer de-
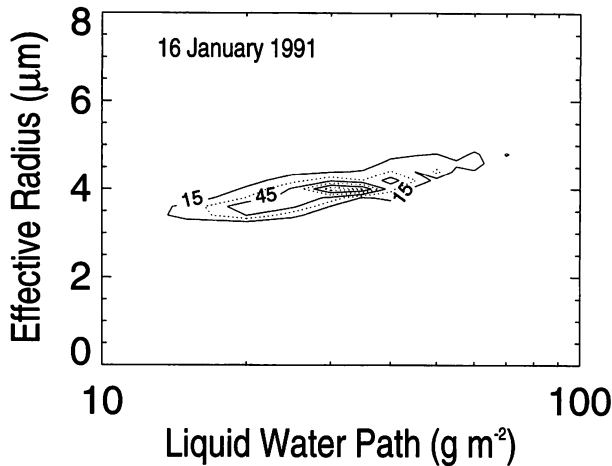
FIG. 8. Effective radius–liquid water path joint probability density function (WENPEX; 16 Jan 1991). Contour levels are 15%, 30%, 45%, 60%, 75%, and 90%.

TABLE 6. Statistics (mean ± standard deviation) of liquid water path.

	Liquid water path (mg cm^{-2})	
	AVHRR* (max)	Microwave** (max)
16 Jan 1991	5.0 ± 3.7 (28.5)	8.9 ± 3.9 (31.2)
18 Jan 1991	4.9 ± 3.3 (21.8)	7.9 ± 5.7 (25.0)
27 Jan 1991	3.0 ± 2.7 (18.3)	3.8 ± 3.2 (20.1)

* AVHRR is spaceborne observation.
** Microwave is airborne observation (above cloud).

using AVHRR GAC data [Han et al. (1994); the Northern Hemisphere case in summer over ocean in Table 6]. The optical thickness of clouds (or the liquid water path) and the effective particle radius also are larger in the FIRE region in summer than in the WENPEX region in winter.

velops, both the effective particle radius and the liquid water path become larger. The thick contour lines of 16 July, on the other hand, show the weak negative correlation between the effective particle radius and the liquid water path. A similar tendency is seen on the part of the larger effective particle radius on 10 July 1987, which was explained as the drizzle-dominated portion (Nakajima et al. 1991). The weak negative correlation in Fig. 10 may be relevant to the process in which more drizzle decreases water amount. It is suggested that the process is a part of the negative feedback of drizzle upon liquid water content; that is, increased water amount results in more drizzle, which decreases the water amount such as by a rainfall process, thereby decreasing the drizzle.

The regional statistics (mean ± standard deviation) of the optical thickness of clouds, the effective particle radius, and the liquid water path in the analyzed region for all three days (7, 10, and 16 July 1987) are summarized in Table 5 together with the WENPEX results. These results for marine stratocumulus off the coast of California in summer are larger for the optical thickness and smaller for the effective particle radius, respectively, in comparison with near-global statistical analyses

5. Discussion

In this section, we will discuss the partial cloud problem that potentially influences the algorithm's validity. It also is pointed out that the horizontal inhomogeneity of the cloud layer, the spatial resolution of the sensor, and other factors may influence the retrieval of several cloud parameters (Loeb and Coakley 1998; Oreopoulos and Davies 1998a,b). We particularly focus on the quantitative comparison of the liquid water path derived from the AVHRR retrieval with the in situ airborne observations in this study. For this purpose, the results in the WENPEX region, in which stratus, stratocumulus, and cumulus existed, are used because they are less homogeneous horizontally than are the results in the FIRE region, in which stratus and stratocumulus dominated.

Comparison between Fig. 11 and Fig. 1 shows that the low-level marine cloud field on 27 January 1991 is less homogeneous horizontally than that of 16 January 1991. The partial cloud influence within the instantaneous FOV (IFOV, i.e., one pixel) is investigated by comparison between the simultaneous flight legs of the Cessna and AVHRR in detail. The flight leg is indicated by the thick white line in Fig. 11. The fourth flight leg is synchronized exactly to the NOAA AVHRR obser-

TABLE 5. Statistics of retrieved results of cloud parameters.

Date	Optical thickness	Effective radius (µm)	Liquid water path (mg cm^{-2})	Correlation coef[a]
16 Jan 1991	16.4 ± 9.73	4.3 ± 0.61	5.0 ± 3.7	0.747
18 Jan 1991	13.9 ± 9.10	5.3 ± 0.73	4.9 ± 3.3	0.009
27 Jan 1991	7.44 ± 6.57	6.3 ± 1.1	3.0 ± 2.7	−0.102
7 Jul 1987	6.9 ± 3.6	7.9 ± 0.88	3.7 ± 2.0	0.461
10 Jul 1987	30.3 ± 9.0	8.0 ± 1.6	15.6 ± 4.0	−0.367[b] (0.538[c])
16 Jul 1987	50.4 ± 11.2	6.7 ± 0.56	22.5 ± 4.5	−0.136

[a] Correlation coefficient is between the effective particle radius and the liquid water path in linear scale.
[b] The correlation coefficient only for effective particle radius greater than or equal to 8 µm.
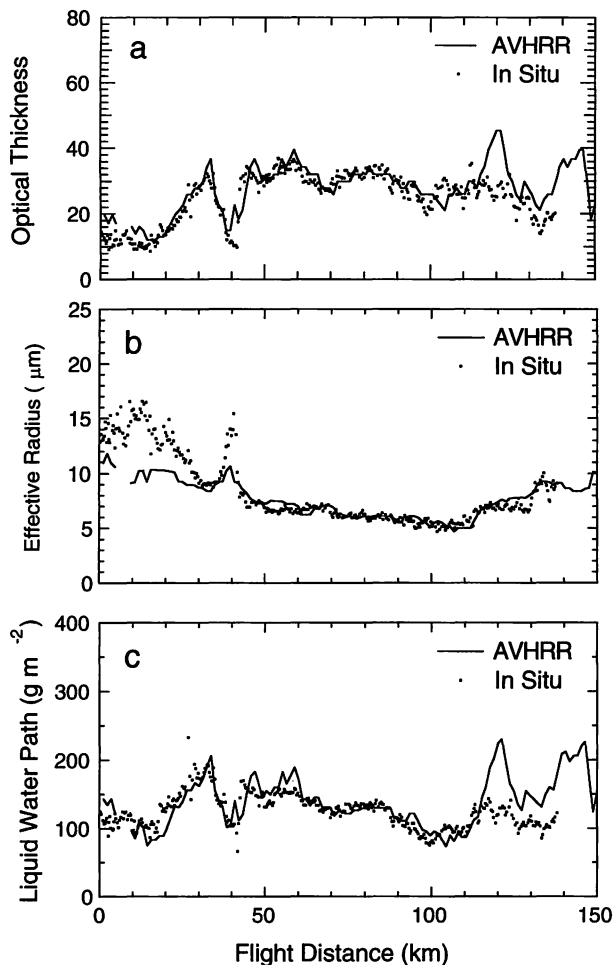[c] The correlation coefficient only for effective particle radius less than 8 µm.

FIG. 9. Validation of the retrieved parameters along the nadir flight leg in the FIRE region (10 Jul 1987). (a) Optical thickness of clouds: solid line shows the retrieved optical thickness from AVHRR, and dots are derived from the microphysical in situ observations. (b) Effective radius of droplets: solid line is adjusted to the central height of the C-131A in situ PMS probe observation (dots). (c) Liquid water path: solid line is the derived effective particle radius adjusted to the center. Johnson–Williams hot-wire probe was used to observe liquid water content. The breaking off at several kilometers of flight distance is due to the original AVHRR data loss.

FIG. 10. Effective radius–liquid water path joint probability density function (FIRE region; 7, 10, and 16 Jul 1987). Contour levels are 10%, 30%, 50%, and 90% for 7 Jul; 10%, 30%, 50%, 70%, and 90% for 16 Jul; and 10%, 20%, 50%, and 90% for 10 Jul. Thicker lines are used for 16 Jul 1987.

vations temporally and spatially. Figure 12 shows the comparison between the retrieved results and the in situ observations. Figure 12a shows the longitudinal profile of the effective particle radius retrieved from AVHRR and that observed by FSSP on board the Cessna (aircraft B). This observation flight was performed at about the cloud-top level, and the effective particle radius retrieved from AVHRR was adjusted to the cloud-top level. Figure 12b is the liquid water path variation derived from AVHRR and microwave radiometry from the Cessna (aircraft A). Figure 12c is the infrared ch.-4 brightness temperature variation. The cloud field along the flight leg is inferred to be very inhomogeneous horizontally because of the following consideration. The cloud-top and -bottom heights were estimated by human
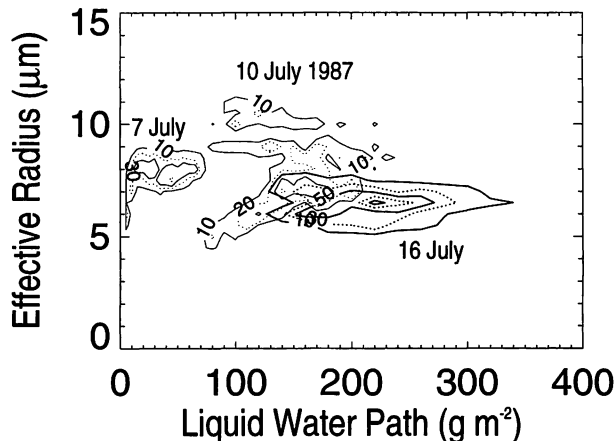
observation from the aircraft. The air temperature at the cloud top was near 269 K and that of the cloud bottom was near 274 K, estimated from the Naze Observatory of the Japan Meteorological Agency, which is about 100 km away from the observation area. The climatic value of the sea surface temperature in the analyzed region was about 20°C (or near 293 K). The range of the brightness temperature in Fig. 12c was about 272–284 K. This range indicates that the AVHRR scanned the cloud and sea surface in the IFOV, and the cloud layer appeared to be horizontally inhomogeneous. It is shown in Fig. 12a that the retrieved results and in situ observations have almost the same order of magnitude, but the variation is out of phase between them. This result seems to be ascribable to the convective-cloud horizontal inhomogeneity. A plane-parallel cloud layer is assumed in the retrieval model atmosphere. In the case that one pixel contains both cloud and sea in its IFOV, the observed radiance will be lower than that fully covered by cloud. As a result, the retrieved effective droplet particle radius appears to be larger than the true value (cf. Fig. 5). Larger effective droplet radii apparently were retrieved for the region of higher brightness temperature near 128.8° and 128.9°E. Furthermore, the variation of the in situ FSSP observation in Fig. 12a suggests that the effective particle radius is larger at the multiple convective cells (e.g., near 128.80° to 128.85°E identified as a larger–liquid water path region the microwave radiometry observation in Fig. 12b) than at either the edge of them or the interstitial region (e.g., near 128.910°E identified as a very little–liquid water path region in Fig. 12b). This tendency also corresponds to the brightness temperature variation in Fig. 12c. That is, greater variation in the brightness temperature in Fig. 12c corresponds to greater difference between the AVHRR-retrieved effective particle radius and the in situ effective particle radius. With respect to the liquid
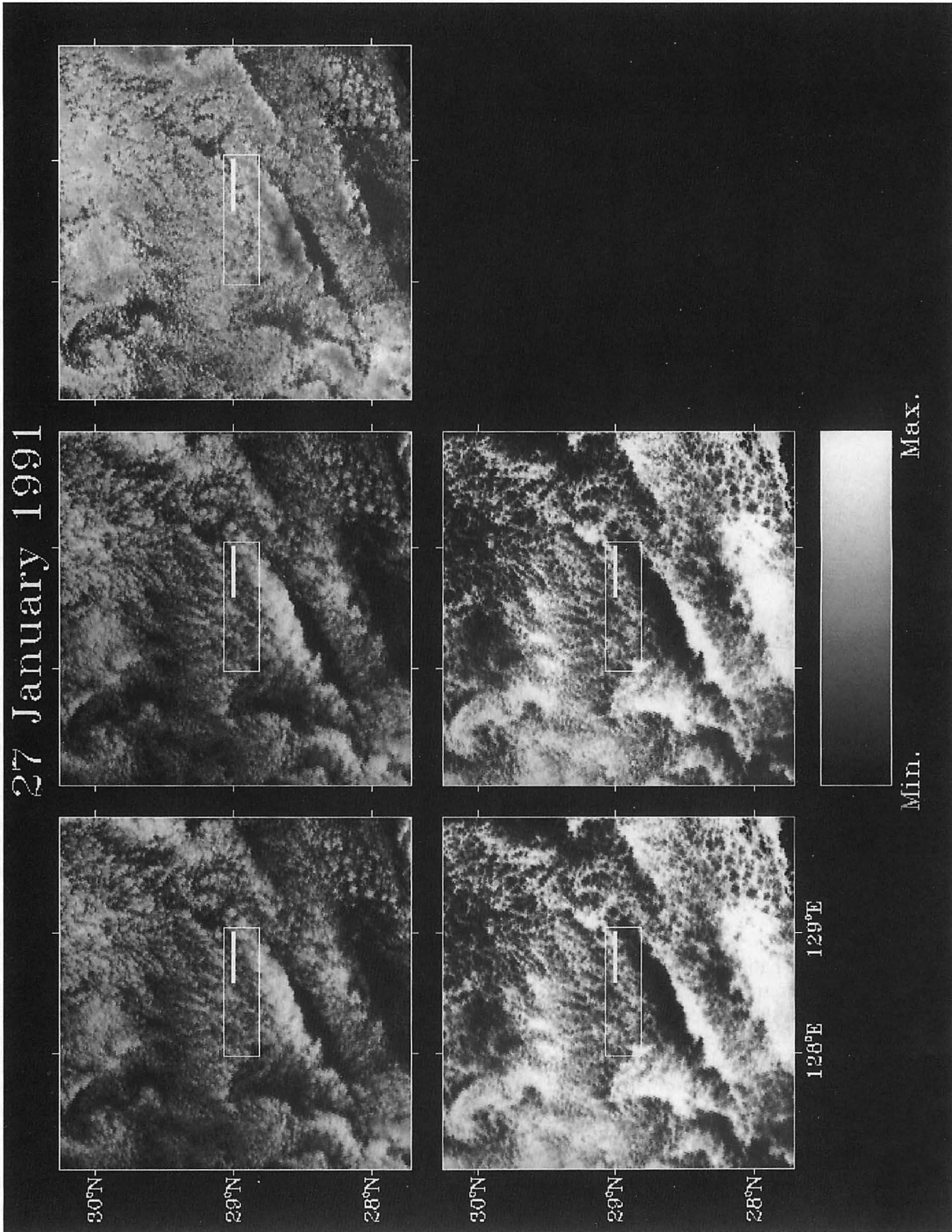
FIG. 11. Imagery of AVHRR data (27 Jan 1991). As in Fig. 1 but for 27 Jan 1991. Center frame of each image indicates the analyzed area (27 × 95 pixels on this date). The straight lines in the analyzed areas illustrate the flight lines of in situ airborne observations.
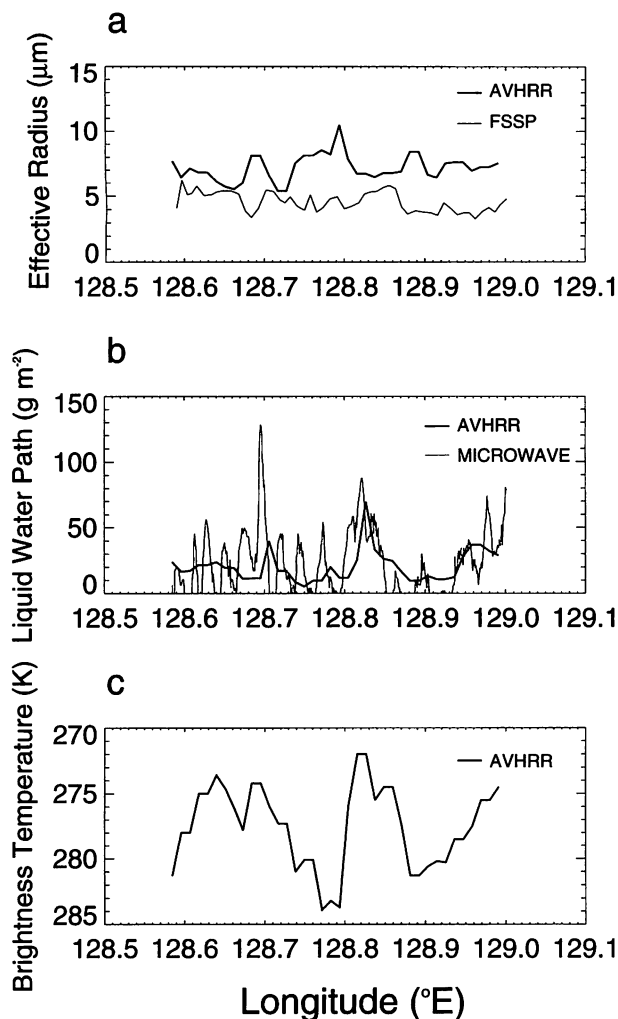
a

Effective Radius (μm)

b

Liquid Water Path (g m⁻²)

c

Brightness Temperature (K)

Longitude (°E)

FIG. 12. Validation of the retrieved parameters along the flight leg in the WENPEX region (27 Jan 1991). (a) Effective radius of droplets: thicker line is the retrieved effective particle radius adjusted to the cloud-top level, and thinner line is the Cessna 404 in situ FSSP observation at the cloud top in level flight. (b) Liquid water path: thicker line was derived using the retrieved effective particle radius adjusted to the cloud-middle level, and thinner line is the result of microwave radiometry observation. (c) Brightness temperature: AVHRR ch.-4 brightness temperature with a longitudinal profile.

Probability Density Function

a

b

c

Liquid Water Path (mg cm⁻²)

FIG. 13. Probability density function for liquid water path (WEN-PEX). (a) 16 Jan 1991: thicker line is the AVHRR results, and thinner line is the microwave radiometry. (b) As in (a) but for 18 Jan 1991. (c) As in (a) but for 27 Jan 1991.

water path, the variation of the results derived from AVHRR and microwave radiometry indicates a similar tendency due to the cloud horizontal inhomogeneity. The microwave radiometry from the Cessna shows fine and dynamic variation because of its small IFOV (about 4°; about 40 m in situ). The AVHRR result, on the other hand, shows the average variation of that derived from the microwave radiometry because its larger IFOV (about a few kilometers in situ).

The comparison of the liquid water path also is discussed from a statistical point of view. Table 6 summarizes the statistics of the liquid water path for the WENPEX region. Some bias exists between the mean liquid water path derived from AVHRR and that of mi-
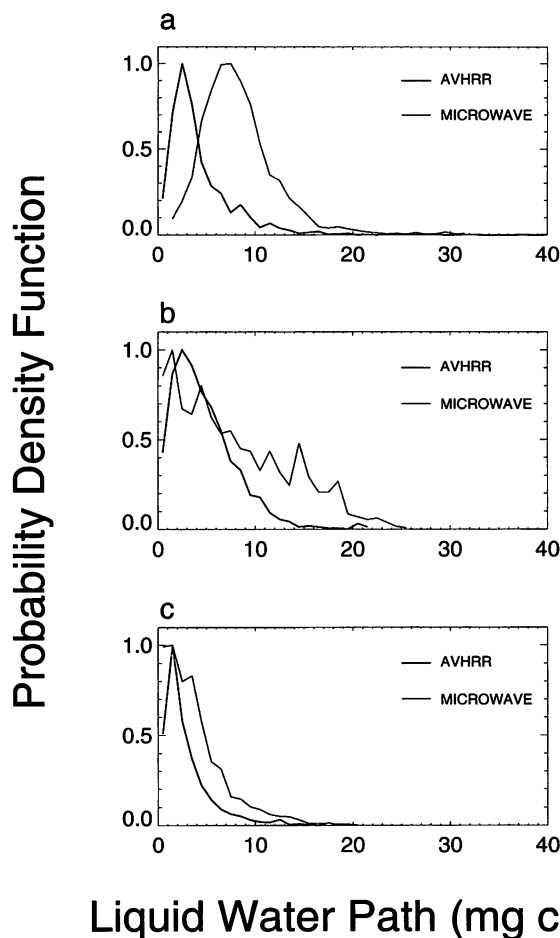
crowave radiometry. This discrepancy may be ascribed to the following reason. The statistics from microwave radiometry are apt to be taken from the data in which only cloud exists within the smaller range of IFOV rather than from AVHRR, which tends to observe the radiance averaged on both cloudy and noncloudy regions (i.e., sea surface) in the same pixel. Smaller mean values therefore were retrieved from AVHRR than from microwave radiomerry over all three days. This fact is not sufficient, however, to explain the statistical inconsistency in Table 6. Figure 13 illustrates the probability density function of the liquid water path for the analyzed area of AVHRR and for all flights with microwave radiometry, respectively. The shape of the probability density function of AVHRR shifts to a smaller portion than that of the microwave radiometry on 16 January 1991 (Fig. 13a), but both shapes are also very smooth because of the horizontal homogeneity of the cloud layer on this day. These features of the shapes can be explained by the characteristics of the retrieval algorithm for microwave radiometry. The retrieval algorithm of the liquid
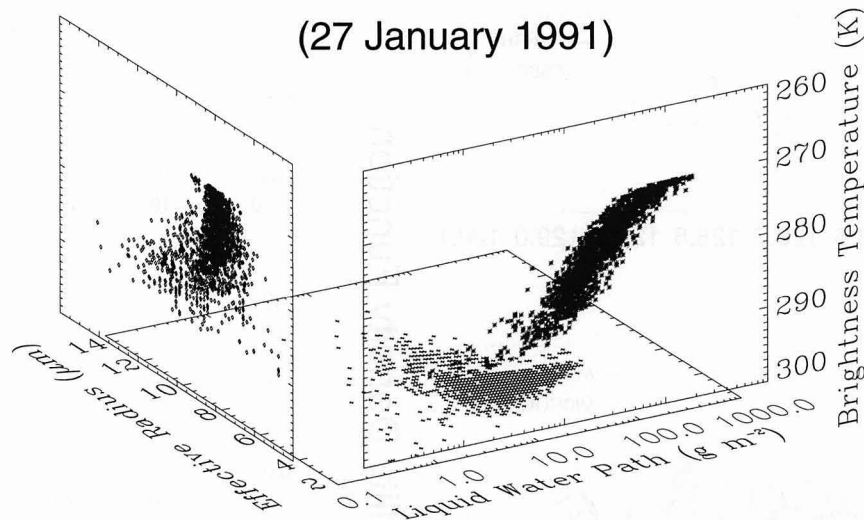
FIG. 14. Composite of results along the Cessna observed area on 27 Jan 1991. (bottom panel) The relationship between the derived liquid water path and the retrieved effective particle radius. (right front panel) The relationship between the liquid water path and the brightness temperature in ch. 4. (left front panel) The relationship between the effective particle radius and the brightness temperature in ch. 4. The range of the brightness temperature decreases in the upper portion of the ordinate.

water path from the microwave radiometry is based upon Takeda and Liu (1987). This algorithm, in principle, uses the brightness temperature of the sea surface as the reference and the difference between the observed brightness temperature above the cloud and the reference to retrieve a liquid water path. The larger liquid water path therefore is derived from the larger difference of the brightness temperature. On 16 January 1991, the airborne observation area was overcast so that we could not determine exactly the reference brightness temperature for the sea surface. A more erroneous value is obtained when the difference in brightness temperature between clouds and the reference (sea surface) is small, that is, the liquid water path is small. That reason is why the bias in the small–liquid water path portion between the AVHRR shape and the microwave shape is larger on 16 January 1991 than on the other two days, in spite of the fact that they are essentially the same shape. For the other two days, on the other hand, the shapes of the probability density functions are not similar between AVHRR and microwave radiometry, and statistical values are not so consistent because of the horizontal inhomogeneity. We further compared the retrieved liquid water path with that derived from microwave radiometry with respect to the maximum value in the WENPEX region, as discussed by Fujiyoshi et al. (1995). The idea of the maximum value comparison is based on the principle that a fully developed cloud system has a liquid water path of maximum value predicted by adiabatic air conditions. The maximum values for the three days are also shown in parentheses in Table 6, which indicates the consistency between the AVHRR

results and the microwave results rather than the mean value comparison.

The partial cloud influences on wider-area retrieval were investigated. Figure 14 shows the composite results of the effective particle radius, the liquid water path, and the infrared brightness temperature for 27 January 1991. This figure indicates that there are pixels that contain not only clouds but also the sea surface in the analyzed area. They have specifications that differ from those of the horizontally homogeneous marine stratocumulus clouds such as those seen in 16 January 1991 and 10 July 1987 data, that is, lower liquid water path, higher effective particle radius, and higher brightness temperature. The air temperature range on this day was determined to be from 269 (cloud-top height) to 274 K (cloud-bottom height), as was discussed above. The brightness temperature range in Fig. 14 is about 270–290 K. This range indicates that the analyzed area contains pixels that clearly show the sea surface. This situation causes errors in the retrieval algorithm because the model atmosphere corresponds to pixels fully covered by cloud layers. For comparison, we took an example from the FIRE region cases. Figure 15 also shows the composite results of the effective particle radius, liquid water path, and brightness temperature for 10 July 1987. The brightness temperature range is about 3 K, and this range is consistent with the air temperature difference between the top and the bottom of the cloud layer suggested from radiosonde observations (Nakajima et al. 1991). Cloud fields in this case were suitable for the plane-parallel model atmosphere, which meant that good consistency was obtained between the re-

Composite of Results (LWP, r_e, and T_{bb4})
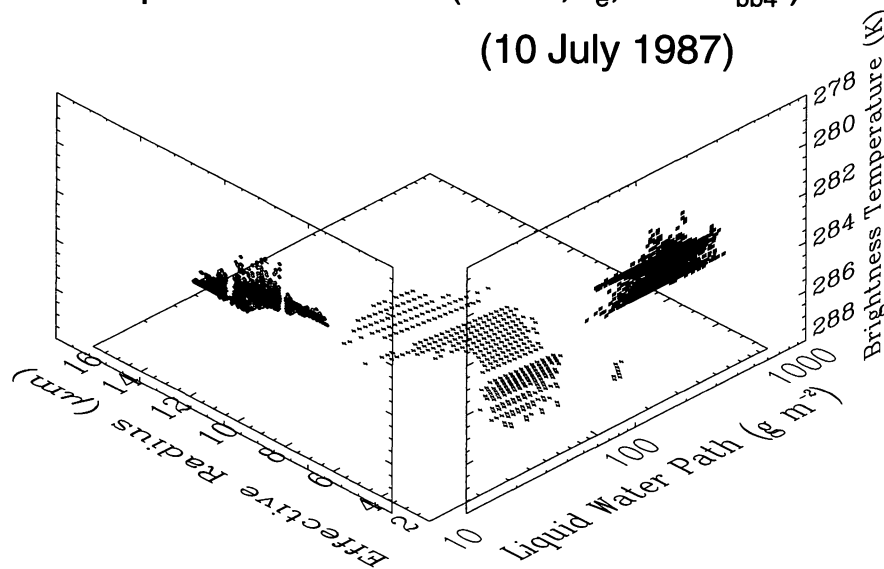## (10 July 1987)

FIG. 15. As in Fig. 14 but for the retrieved results for the analyzed area on 10 Jul 1987. This case is more horizontally homogeneous than that of 27 Jan 1991 (Fig. 14).

trieved cloud parameters from AVHRR and those from in situ observations seen in Fig. 9.

6. Concluding remarks

An algorithm was developed to retrieve the optical thickness, effective particle radius, and vertically integrated liquid water content for low-level marine clouds from NOAA AVHRR LAC data. The algorithm uses the visible (ch. 1) and the middle-infrared (ch. 3) reflected radiance as well as the thermal infrared (ch. 4) to correct the thermal component of the middle infrared. The correction methodology in this study utilizes a regression curve between ch. 3 and ch. 4 for thermal radiation emitted from the earth–atmosphere system that is based on the spatial coherence method (Coakley and Bretherton 1982), but the radiative transfer calculations and iterative retrieval approach were adopted for this correction by Nakajima and Nakajima (1995).

This algorithm was applied to the data of an area in which almost-synchronized airborne observations were performed during FIRE and WENPEX IFO. The retrieved results were compared with the in situ and remote-sensing airborne observations to validate this algorithm. There are several differences in the cloud types between FIRE and WENPEX, that is, the horizontally very homogeneous cloud systems such as stratus or stratocumulus for the FIRE region in the northeast Pacific in summer and the mostly horizontally inhomogeneous system such as cumulus for the WENPEX region over the East China Sea in winter.

As a result, for the FIRE region, the optical thickness of cloud, the effective particle radius, and the liquid water path retrieved from AVHRR are consistent with

the in situ airborne observations. The results for the WENPEX region, on the other hand, show some discrepancies in the effective particle radius and the liquid water path, when compared with the corresponding in situ airborne observations in the detailed and statistical analysis of the horizontally inhomogeneous cloud system. The consistency between the results from AVHRR and the results from in situ observations, however, is good when the low-level clouds are horizontally homogeneous for the FIRE and WENPEX regions. It is shown from comparison with airborne observations that the algorithm developed in this study can be applied effectively to fully cloud-covered pixels. For the partially cloud-covered pixels, however, the retrieved results have some biases; that is, there is a tendency to estimate the optical thickness and liquid water paths as being smaller and the effective particle radii as being larger than those of fully cloud-covered cases. These results indicate that the partial-cloud effect should be taken into consideration in regional and global analysis that includes several types of cloud and, in particular, uses larger IFOV remotely sensed data from larger areas, such as that from AVHRR GAC. It further is suggested that the thermal-infrared channel, which is used only to remove the thermal component from the middle-infrared radiance, has a potential to provide additional information about the inhomogeneity of cloud fields as a result of the detailed analyses of stratus and broken cloud fields in the FIRE and WENPEX regions.

REFERENCES

Albrecht, B. A., D. A. Randall, and S. Nicholls, 1988: Observations of marine stratocumulus clouds during FIRE. *Bull. Amer. Meteor. Soc.,* **69,** 618–626.

Arking, A., and J. D. Childs, 1985: Retrieval of cloud cover parameters from multispectral satellite images. *J. Climate Appl. Meteor.,* **24,** 322–333.

Coakley, J. A., Jr., and F. R. Bretherton, 1982: Cloud cover from high-resolution scanner data: Detecting and allowing for partially filled fields of view. *J. Geophys. Res.,* **87,** 4917–4932.

——, and R. Davies, 1986: The effect of cloud sides on reflected solar radiation as deduced from satellite observations. *J. Atmos. Sci.,* **43,** 1025–1035.

Curran, R. J., and M.-L. C. Wu, 1982: Skylab near-infrared observations of clouds indicating supercooled liquid water droplets. *J. Atmos. Sci.,* **39,** 635–647.

Downing, H. D., and D. Williams, 1975: Optical constants of water in the infrared. *J. Geophys. Res.,* **80,** 1656–1661.

Fujiyoshi, Y., Y. Ishizaka, T. Takeda, T. Hayasaka, and M. Tanaka, 1995: Measurement of vertical liquid water path by means of an airborne radiometer and the shortwave albedo of marine low-level clouds during WENPEX in Japan. *J. Appl. Meteor.,* **34,** 471–481.

Hale, G. M., and M. R. Querry, 1973: Optical constants of water in the 200-nm to 200-μm wavelength region. *Appl. Opt.,* **12,** 555–563.

Han, Q., W. B. Rossow, and A. A. Lacis, 1994: Near-global survey of effective droplet radii in liquid water clouds using ISCCP data. *J. Climate,* **7,** 465–497.

Hansen, J. E., and J. B. Pollack, 1970: Near-infrared light scattering by terrestrial clouds. *J. Atmos. Sci.,* **27,** 265–281.

——, and L. D. Travis, 1974: Light scattering in planetary atmospheres. *Space Sci. Rev.,* **16,** 527–610.

Hayasaka, T., M. Kuji, and M. Tanaka, 1994: Air truth validation of cloud albedo estimated from NOAA Advanced Very High Resolution Radiometer data. *J. Geophys. Res.,* **99,** 18 685–18 693.

——, N. Kikuchi, and M. Tanaka, 1995: Absorption of solar radiation by stratocumulus clouds: Aircraft measurements and theoretical calculations. *J. Appl. Meteor.,* **34,** 1047–1055.

Ishizaka, Y., Y. Kurahashi, and H. Tsuruta, 1995: Microphysical properties of winter stratiform clouds over the southeast islands area in Japan. *J. Meteor. Soc. Japan,* **73,** 1137–1151.

Kidwell, K. B., 1991: NOAA Polar Orbiter Data User's Guide (*TIROS-N, NOAA-6, NOAA-7, NOAA-8, NOAA-9, NOAA-10, NOAA-11,* and *NOAA-12*). NOAA Tech. Note, 294 pp. [Available from NOAA/NESDIS/National Climatic Data Center, Sat-

ellite Data Services Division, Princeton Executive Square, Room 100, Washington, DC 20233; also available online at http://www2.ncdc.noaa.gov/docs/podug/index.htm.]

Loeb, N. G., and J. A. Coakley Jr., 1998: Inference of marine stratus cloud optical depths from satellite measurements: Does 1D theory apply? *J. Climate,* **11,** 215–233.

Los, S. O., 1993: Calibration adjustment of the NOAA AVHRR Normalized Difference Vegetation Index without recourse to component channel 1 and 2 data. *Int. J. Remote Sens.,* **14,** 1907–1917.

Nakajima, T., and M. Tanaka, 1986: Matrix formulation for the transfer of solar radiation in a plane-parallel scattering atmosphere. *J. Quant. Spectrosc. Radiat. Transfer,* **35,** 13–21.

——, and ——, 1988: Algorithms for radiative intensity calculations in moderately thick atmospheres using a truncation approximation. *J. Quant. Spectrosc. Radiat. Transfer,* **40,** 51–69.

——, and M. D. King, 1990: Determination of the optical thickness and effective particle radius of clouds from reflected solar radiation measurements. Part I: Theory. *J. Atmos. Sci.,* **47,** 1878–1893.

——, ——, J. D. Spinhirne, and L. F. Radke, 1991: Determination of the optical thickness and effective particle radius of clouds from reflected solar radiation measurements. Part II: Marine stratocumulus observations. *J. Atmos. Sci.,* **48,** 728–750.

Nakajima, T. Y., and T. Nakajima, 1995: Wide-area determination of cloud microphysical properties from NOAA AVHRR measurements for FIRE and ASTEX regions. *J. Atmos. Sci.,* **52,** 4043–4059.

Oreopoulos, L., and R. Davies, 1998a: Plane parallel albedo biases from satellite observations. Part I: Dependence on resolution and other factors. *J. Climate,* **11,** 919–932.

——, and ——, 1998b: Plane parallel albedo biases from satellite observations. Part II: Parameterizations for bias removal. *J. Climate,* **11,** 933–944.

Pierluissi, J. H., and C.-M. Tsai, 1987: New LOWTRAN models for the uniformly mixed gases. *Appl. Opt.,* **26,** 616–618.

——, C. E. Maragoudakis, and R. Tehrani-Movahed, 1989: New LOWTRAN band model for water vapor. *Appl. Opt.,* **28,** 3792–3795.

Platnick, S., and S. Twomey, 1994: Determining the susceptibility of cloud albedo to changes in droplet concentration with the Advanced Very High Resolution Radiometer. *J. Appl. Meteor.,* **33,** 334–347.

Rawlins, F., and J. S. Foot, 1990: Remotely sensed measurements of stratocumulus properties during FIRE using the C130 aircraft multi-channel radiometer. *J. Atmos. Sci.,* **47,** 2488–2503.

Stephens, G. L., 1978: Radiation profiles in extended water clouds. II: Parameterization schemes. *J. Atmos. Sci.,* **35,** 2123–2132.

Takeda, T., and G. Liu, 1987: Estimation of atmospheric liquid-water amount by *Nimbus 7* SMMR data: A new method and its application to the western North Pacific region. *J. Meteor. Soc. Japan,* **65,** 931–947.

Taylor, J. P., 1992: Sensitivity of remotely sensed effective radius of cloud droplets to changes in LOWTRAN version. *J. Atmos. Sci.,* **49,** 2564–2569.

Teillet, P. M., P. N. Slater, Y. Ding, R. P. Santer, R. D. Jackson, and M. S. Moran, 1990: Three methods for the absolute calibration of the NOAA AVHRR sensors in-flight. *Remote Sens. Environ.,* **31,** 105–120.

Thekaekara, M. P., 1974: Extraterrestrial solar spectrum, 3000–6100 Å at 1-Å intervals. *Appl. Opt.,* **13,** 518–522.

Twomey, S., and T. Cocks, 1982: Spectral reflectance of clouds in the near-infrared: Comparison of measurements and calculations. *J. Meteor. Soc. Japan,* **60,** 583–592.